Available online at www.sciencedirect.com
SCIENCE DIRECT®
International Journal of Heat and Fluid Flow 24 (2003) 210–222
International Journal of HEAT AND FLUID FLOW
www.elsevier.com/locate/ijhff

Heat transfer mechanisms in vapor mushroom region of saturated nucleate pool boiling

J.J. Wei [a,*], B. Yu [a], H.S. Wang [b]

[a] Turbomachinery Research Group, Institute for Energy Utilization, National Institute of Advanced Industrial Science and Technology, 1-2 Namiki, Tsukuba, Ibaraki 305-8564, Japan
[b] Department of Engineering, Queen Mary, University of London, London E1 4NS, UK

Received 22 February 2002; accepted 9 December 2002

Abstract

To reveal the highly efficient heat transfer mechanisms in the vapor mushroom region of saturated nucleate pool boiling, a new model was developed in which three heat transfer mechanisms were considered: the conduction and evaporation in the microlayer region underneath vapor stem, the conduction and evaporation in the macrolayer region between the vapor mushroom and the heater surface and Marangoni convection in the macrolayer region. Two-dimensional conservation equations for laminar flow in the macrolayer region and conduction in the heater were solved. The SIMPLE-algorithm was used for handling the pressure–velocity coupling. Calculated boiling curve agrees well with the published experimental data and numerical results showed that about 60% heat flux is transferred by evaporation in the microlayer region, and about 40% heat flux is evaporated at the vapor–liquid interfaces of the macrolayer due to both the conduction and Marangoni convection heat transfer in the macrolayer region. Further investigations were also carried out for the cases in which only one or two heat transfer mechanisms were considered to assess the relative influences of the microlayer evaporation and Marangoni convection.

Keywords: Pool boiling; Microlayer; Macrolayer; Marangoni convection

1. Introduction

Nucleate boiling is favored in electronic devices cooling, refrigeration, air-conditioning and many other industrial applications due to its highly efficient heat transfer performance. Typical nucleate boiling regions on a classical boiling curve of heat flux versus wall superheat were classified in the pioneering study of Gaertner (1965) as incipient boiling, discrete bubble region, first transition region, vapor mushroom region, second transition region and critical heat flux (CHF) point. Of these subregions of nucleate boiling, the high heat flux vapor mushroom region has been given a significant study. The vapor mushroom region is characterized by the formation of a liquid layer interspersed with numerous, continuous columnar vapor stems underneath a growing mushroom-shaped bubble shown in Fig. 1. The liquid layer between the vapor mushroom and the heater surface has been termed as the macrolayer, whereas the thin liquid film formed underneath vapor stems is known as the microlayer. In addition to the visual observations of Gaertner (1965), Iida and Kobayasi (1969) and Bhat et al. (1986) confirmed the existence of a liquid-rich layer near the heated surface through the measurements of void fraction profiles near the heater surface using an electrical conductivity probe.

To understand the complicated heat transfer mechanisms in the vapor mushroom region of nucleate boiling is one of the most challenging problems of heat transfer. Many studies have been tried to establish a physical model to explain the highly efficient heat transfer mechanisms by using the macrolayer and microlayer conceptions. A transient 1D model of the macrolayer evaporation phenomena was proposed in Bhat et al. (1983a,b, 1986) and Jairajpuri and Saini (1991), which regards the conduction across the macrolayer and evaporation from the top interface of the macrolayer as

* Corresponding author. Tel.: +81-298-61-7257; fax: +81-298-61-7275.
E-mail address: wei-jinjia@aist.go.jp (J.J. Wei).

0142-727X/03/$ - see front matter © 2003 Elsevier Science Inc. All rights reserved.
doi:10.1016/S0142-727X(02)00244-8

Nomenclature

A	area (m^2)
c_p	heat capacity ($J\,kg^{-1}\,K^{-1}$)
E	evaporation coefficient
f	fraction of evaporation
g	gravitational acceleration ($m\,s^{-2}$)
h	heat transfer coefficient ($W\,m^{-2}\,K^{-1}$)
h_{fg}	latent heat of evaporarization ($J\,kg^{-1}$)
k	thermal conductivity ($W\,m^{-1}\,K^{-1}$)
m	mass evaporation of the triple-point ($kg\,s^{-1}\,m^{-1}\,K^{-1}$)
M	molecular weight ($kg\,kmol^{-1}$)
Ma	Marangoni number
N	number of vapor stems
p	pressure ($N\,m^{-2}$)
q	heat flux ($W\,m^{-2}$)
Q	heat transfer rate (W)
r_v	radius of vapor stem (m), Fig. 2
r_l	radius of computational cell (m), Fig. 2
R	universal gas constant ($J\,kmol^{-1}\,K^{-1}$)
T	temperature (°C)
v	fluid velocity component in r direction ($m\,s^{-1}$)
w	fluid velocity component in z direction ($m\,s^{-1}$)
r	coordinate along the heated wall (m), Fig. 2
z	coordinate perpendicular to the heated wall (m), Fig. 2

Greeks

α	thermal diffusivity ($m^2\,s^{-1}$)
β	thermal expansion coefficient (K^{-1})
δ	macrolayer thickness (m)
Δ	heater thickness (m)
μ	dynamic viscosity ($kg\,m^{-1}\,s^{-1}$)
ρ	fluid density ($kg\,m^{-3}$)
σ	surface tension ($N\,m^{-1}$)

Subscripts

bubble	bubble–liquid interface
evap	evaporation
l	liquid
s	heater
sat	saturated
stem	stem–liquid interface
TP	triple-point
v	vapor
w	heater upper surface

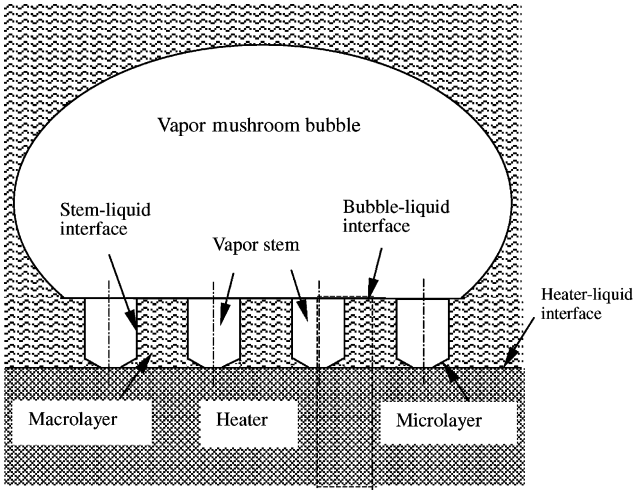

Fig. 1. Schematic of vapor mushroom structure near heated surface.

the dominant heat transfer mechanism; whereas Pan et al. (1989) assumed that the evaporation near the vapor stem dominates the nucleate boiling heat transfer, which is in accordance with the conjecture of Gaertner (1965). Pan and Lin (1989) enhanced the effective liquid thermal conductivity by considering Maragoni-induced flow effects within the macrolayer in their semi-theoretical pseudo-conduction model, and their results showed that about 97% of the heat flux is evaporated at the top surface of the macrolayer. Recently Ma and Pan (1999a,b) abandoned the artificial enhancement of the liquid thermal conductivity in Pan and Lin (1989) and numerically studied the Marangoni-induced thermo-capillary driven flow and heat transfer within the macrolayer region. The numerical results indicated that the thermo-capillary driven flow in the macrolayer region and evaporation at the vapor–liquid interface constitute a very efficient heat transfer mechanism. However, the wall superheat was overpredicted as compared to the experimental data of Gaertner (1965) and Nishikawa et al. (1984). They attributed the overprediction to the relatively thick macrolayer, large cell width based on the model of Haramura and Katto (1983) and not considering the reduction of macrolayer thickness and/or width due to the evaporation at the vapor–liquid interface during the hovering period of a mushroom bubble. However, the macrolayer thickness they used is less than half of the experimental data of Bhat et al. (1986) and the evaporation of the macrolayer is not very large which will be shown in our later analysis. All these indicate that maybe some other important heat transfer mechanisms are overlooked in their model. Chyu (1989) attributed the evaporation of macrolayer to a much thinner microlayer existing under the vapor stem, which plays a major role in the heat transfer. However, Chyu's microlayer hypothesis (Chyu, 1989) of a continuous liquid layer underneath the vapor stem was doubted by Pasamehmetoglu et al. (1993) due to the experimental

observations of a dry spot at the center of the vapor stem. By introducing a liquid–vapor–solid contact point/circle (triple-point) evaporation to consider microlayer evaporation hypothesis, Pasamehmetoglu et al. (1993) developed a transient 2D conduction-dominated model. Their numerical results showed that the dominant evaporation occurs at the liquid–vapor–solid contact point. The transport processes occurring in a vapor stem were modeled and analyzed numerically by Lay and Dhir (1995). They conjectured that heat from the wall is conducted into the macrolayer surrounding the vapor stem and microlayer lying between the heater and the vapor–stem interface and is utilized in evaporation at the liquid–vapor interface.

The major heat transfer mechanisms in the above studies can be summarized as (1) the conduction and evaporation heat transfer in the macrolayer region, (2) the conduction and evaporation heat transfer in the microlayer region, and (3) convective heat transfer in the macrolayer region induced by the Marangoni action at the liquid–vapor interface. While all of these factors maybe play major roles in the heat transfer, only one or two of them were considered in the aforementioned models. Thus a unified answer to the dominant evaporation is not obtained and still hotly debated. The present study is aimed at developing a more detailed physical model by considering these factors functioning simultaneously with different weights to reveal the highly efficient heat transfer mechanisms in the vapor mushroom region of nucleate boiling. In what follows, the model used in the current study is described first. Then the numerical results obtained from the model are presented and relative contributions of every heat transfer mechanism in the current model are studied. Finally, conclusions are drawn.

2. Mathematical model

The vapor stems in mushroom region of the nucleate boiling were assumed to regularly distribute to the surface in the triangular lattice (Ma and Pan, 1999a,b). A unit cell including a central vapor stem surrounded by an equivalent cylindrical macrolayer and the corresponding part of the heater was chosen for analysis, which is enclosed by dash line, as shown in Fig. 1.

The microlayer evaporation plays a very important role in the models of Chyu (1989), Pasamehmetoglu et al. (1993) and Lay and Dhir (1995). Modeling the details of the microlayer would require a true characterization of the curved liquid–vapor interface of the microlayer. The microlayer shape and scale should be influenced by the contact angle between the fluid and the heater surface (Pasamehmetoglu et al., 1993). For simplification purpose, just like Pasamehmetoglu et al. (1993), the microlayer evaporation effect was represented in a lumped

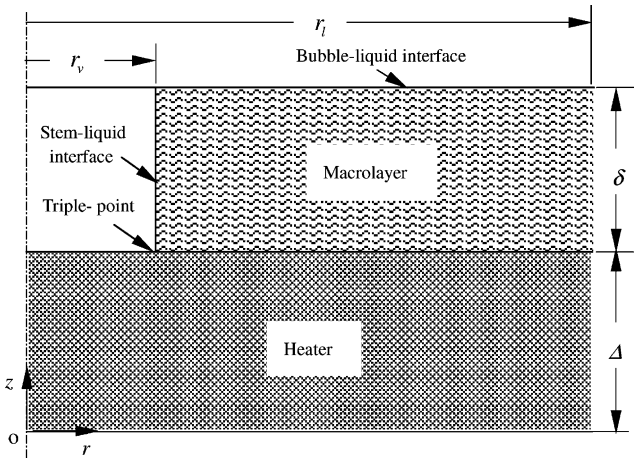

Fig. 2. Computational unit cell.

sense by introducing a liquid–vapor–solid contact point/circle (triple-point) evaporation into the mathematical model as shown in Fig. 2. The interfacial shear stress at the liquid–vapor interface is neglected due to the small density, thermal conductivity and viscosity of vapor as compared with those of the liquid.

For pure liquid, surface tension is a function of temperature and decreases with the increase of temperature. At the vapor–liquid interface, when temperature gradient formed during the heating process, the surface tension gradient is generated, resulting in a tangential shear stress to drive the liquid in the macrolayer to move in the direction of increasing surface tension. This is so-called Marangoni flow. This kind of flow is considered as an effective way to transfer the heat from the heater surface to the vapor–liquid interface for evaporation. The present model consists of the conjugate solution of Marangoni flow and heat transfer in the macrolayer region and the conduction in the heater. The governing equations and boundary conditions will be described later.

The initial conditions for the numerical calculation are difficult to determine. Pasamehmetoglu et al. (1993) assumed that fresh saturated liquid wets the surface at the time of bubble departure and birth of the new bubble. Thus the initial condition of temperature for the macrolayer is saturated and is used at the beginning of every bubble's life. This assumption provides an extreme allowing the maximum effect of liquid resupply as they claimed, whereas the steady state solutions of Ma and Pan (1999a,b) provide the other extreme where the incoming liquid does not disturb the macrolayer. With the assumption that all the heat fluxes are transferred by evaporation, our calculation showed that only 1.2–25.0% of the macrolayer underneath the mushroom bubble is consumed by evaporation during the bubble hovering period at the heat fluxes ranging from 3.0 to 9.0×10^5 $W\,m^{-2}$, which cover the whole vapor mushroom region of nucleate boiling in the experimental data of Gaertner

(1965). Further, the evaporation of macrolayer is much longer than that for the thermo-capillary driven flow through the layer (in the order 10^3) (Ma and Pan, 1999a,b), thus using the steady solutions as Ma and Pan (1999a,b) is a reasonable choice in the present study without the consideration of the reduction of thickness and width of the macrolayer due to evaporation.

2.1. Governing equations

With the assumption of a two-dimensional steady laminar flow and constant properties for the liquid, using Boussinesq assumption to account for buoyancy effects, the governing equations for the liquid macrolayer region are

Continuity equation

$$\frac{1}{r}\frac{\partial(r\rho_l v)}{\partial r}+\frac{\partial(\rho_l w)}{\partial z}=0 \tag{1}$$

Momentum equations

$$\frac{1}{r}\frac{\partial(r\rho_l vv)}{\partial r}+\frac{\partial(\rho_l wv)}{\partial z}=-\frac{\partial p}{\partial r}+\frac{1}{r}\frac{\partial}{\partial r}\left(r\mu_l\frac{\partial v}{\partial r}\right)+\frac{\partial}{\partial z}\left(\mu_l\frac{\partial v}{\partial z}\right)-\mu_l\frac{v}{r^2} \tag{2}$$

$$\frac{1}{r}\frac{\partial(r\rho_l vw)}{\partial r}+\frac{\partial(\rho_l ww)}{\partial z}=-\frac{\partial p}{\partial z}+\frac{1}{r}\frac{\partial}{\partial r}\left(r\mu_l\frac{\partial v}{\partial r}\right)+\frac{\partial}{\partial z}\left(\mu_l\frac{\partial w}{\partial z}\right)+\rho_l\beta g(T-T_{\mathrm{sat}}) \tag{3}$$

Energy equation

$$\frac{1}{r}\frac{\partial(r\rho_l vT)}{\partial r}+\frac{\partial(\rho_l wT)}{\partial z}=\frac{1}{r}\frac{\partial}{\partial r}\left(r\frac{k_l}{c_p}\frac{\partial T}{\partial r}\right)+\frac{\partial}{\partial z}\left(\frac{k_l}{c_p}\frac{\partial T}{\partial z}\right) \tag{4}$$

For the heater, the 2D conduction equation is

$$\frac{1}{r}\frac{\partial}{\partial r}\left(rk_s\frac{\partial T}{\partial r}\right)+\frac{\partial}{\partial z}\left(k_s\frac{\partial T}{\partial z}\right)=0 \tag{5}$$

2.2. Boundary conditions

2.2.1. Axis of the unit computational cell ($r=0$)

The boundary condition at the axis of the unit computational cell can be obtained from the symmetry condition

$$v=0,\quad \frac{\partial w}{\partial r}=0,\quad \frac{\partial T}{\partial r}=0 \tag{6}$$

2.2.2. Heater bottom ($z=0$)

A uniform heat flux boundary condition is used at the bottom of the heater

$$-k_s\frac{\partial T}{\partial z}=q \tag{7}$$

2.2.3. Heater upper surface ($z=\Delta$)

No-slip condition is applied to the impermeable solid surface as

$$v=0,\quad w=0 \tag{8}$$

Underneath the vapor stem ($r<r_v$), the adiabatic boundary condition is used

$$-k_s\frac{\partial T}{\partial z}=0 \tag{9}$$

Underneath the macrolayer ($r_v<r<r_l$), the boundary conditions are as follows:

$$T_{z=\Delta^-}=T_{z=\Delta^+}$$
$$k_s\left(\frac{\partial T}{\partial z}\right)_{z=\Delta^-}=k_l\left(\frac{\partial T}{\partial z}\right)_{z=\Delta^+} \tag{10}$$

The evaporation of the liquid–vapor–solid triple-point can be expressed as [14]

$$Q_{\mathrm{TP}}=m_{\mathrm{TP}}h_{fg}2\pi r_v(T_{\mathrm{TP}}-T_{\mathrm{sat}}) \tag{11}$$

where r_v is the radius of the vapor stem. In the above equation, the triple-point mass evaporation coefficient, m_{TP} ($\mathrm{kg\,s^{-1}\,m^{-1}\,K^{-1}}$), represents the mass of liquid evaporated per unit time per unit perimeter of the vapor stem per degree wall superheat of the triple-point. Physically, m_{TP} models the evaporation of the microlayer shown in Fig. 1.

The other boundary conditions are the same as Ma and Pan (1999a,b), for completeness, they are given here in brief.

2.2.4. Stem–liquid interface ($r=r_v,\ \Delta<z<\Delta+\delta$)

$$v=0,\quad -\mu_l\frac{\partial w}{\partial r}=\frac{\partial\sigma}{\partial T}\frac{\partial T}{\partial z},\quad k_l\frac{\partial T}{\partial r}=h_{\mathrm{evap}}(T-T_{\mathrm{sat}}) \tag{12}$$

where h_{evap} is the heat transfer coefficient due to evaporation and can be approximately expressed as (Ma and Pan, 1999a,b)

$$h_{\mathrm{evap}}=\frac{2E}{2-E}\left(\frac{M}{2\pi R}\right)^{0.5}\frac{h_{fg}^2\rho_v}{T_{\mathrm{sat}}^{1.5}} \tag{13}$$

In the above equation, the evaporation coefficient E has a value varying from 0.02–0.05 (Collier, 1972; Hsu and Graham, 1986; Carey, 1992) to 1 (Kao and Kenning, 1972). The widely differing values of E which have been reported for water is attributed to the impurity of the vapor–liquid interface and cause the difficulty in calculating heat transfer coefficient h_{evap} in Eq. (13). When great care is taken to ensure the purity of the test fluids, E is close to 1. However, E is greatly decreased by

non-condensable gas and impurity at the interface (Kao and Kenning, 1972). Since extreme purity is unlikely in most engineering systems, the value of E is far less than 1 (Carey, 1992). As claimed by Ma and Pan (1999a), a value of 0.04 is regarded as a common value used in the literature. A value of E range from 0.02 to 0.04 was also recommended in the handbook (Paul, 1962). Therefore, considering the actual conditions in most engineering systems, a value of 0.04 given by Ma and Pan (1999a) for water was adopted in the present study.

2.2.5. Bubble–liquid interface ($z = \Delta + \delta$)

$$w = 0, \quad \mu_l \frac{\partial v}{\partial z} = \frac{\partial \sigma}{\partial T}\frac{\partial T}{\partial r}, \quad -k_l \frac{\partial T}{\partial z} = h_{evap}(T - T_{sat}) \tag{14}$$

2.2.6. Unit cell boundary ($r = r_l$)

$$v = 0, \quad \frac{\partial w}{\partial r} = 0, \quad \frac{\partial T}{\partial r} = 0 \tag{15}$$

In Eqs. (1)–(15), Eqs. (1)–(5) are the coupled continuity, momentum and energy equations for describing the flow and conductive/convective heat transfer in the macrolayer region. The surface tension gradient at the vapor–liquid interface of the macrolayer region generates the Marangoni flow, and is given in Eqs. (12) and (14) as boundary conditions for the solution of the Marangoni flow. Also the evaporation heat transfer at the vapor–liquid interface is defined in Eqs. (12) and (14) as boundary conditions for the solution of conductive/convective heat transfer in the macrolayer region. The microlayer evaporation heat transfer is given by Eq. (11). The other equations are subsidiary equations for the closure of Eqs. (1)–(5). Thus Eqs. (1)–(15) constitute our new model, and the current model considers the three heat transfer mechanisms mentioned in the Introduction section.

2.3. Solution domain dimensions

For the numerical computation of the model equations, a solution domain must be specified, which includes the inner radius of the macrolayer (radius of vapor–stem), r_i, the outer radius of the macrolayer, r_l, and the thickness of the macrolayer, δ.

Here, saturated water was selected for the computations since the macrolayer thickness and number density of stem were measured in some experiments (Gaertner, 1965; Iida and Kobayasi, 1969; Bhat et al., 1986). Pasamehmetoglu and Nelson (1987) gave a detail review on the macrolayer thickness and proposed a correlation which agrees well with the experimental data of Bhat et al. (1986). The correlation of Haramura and Katto (1983) employed by Ma and Pan (1999a,b) predicts a macrolayer thickness less than half of the experimental data of Bhat et al. (1986). Haramura and Katto (1983) were primarily concerned with developing a new CHF model and arbitrarily postulated the macrolayer thickness to be one-fourth of the Helmholtz instability wavelength. Consequently, their study includes little detail concerning the macrolayer thickness and lacks experimental support (Pasamehmetoglu and Nelson, 1987). Therefore, the correlation of Pasamehmetoglu and Nelson (1987) was preferred in the present study, which is expressed as

$$\delta = \frac{\pi}{2}\sigma\left(\frac{A_v}{A_w}\right)^2\left(\frac{\rho_l + \rho_v}{\rho_l \rho_v}\right)\left(\frac{\rho_v h_{fg}}{q}\right)^2 \tag{16}$$

where A_v/A_w is the fraction of the heated surface area occupied by vapor stems and can be expressed as (Pasamehmetoglu and Nelson, 1987)

$$\frac{A_v}{A_w} = \left(\frac{r_v}{r_l}\right)^2 = C_A q^{1/4} \tag{17}$$

where $C_A = 6.206 \times 10^{-4}\ \mathrm{W^{-1/4}\,m^{1/2}}$.

To estimate the stem radius and the corresponding heater radius for an average stem, the following relationship between the population density of stem and heat flux proposed by Gaertner (1965) was used in the present model:

$$q = C_N\left(\frac{N}{A_w}\right)^{2/3} \tag{18}$$

where $C_N = 117.1\ \mathrm{W\,m^{-2/3}}$.

Thus the dimensions of solution domain can be determined by Eqs. (16)–(18). Eq. (16) gives the thickness of the macrolayer, δ, while the combination of Eqs. (17) and (18) gives the inner and outer radius of the macrolayer, r_i and r_l, at a given heat flux.

From the experimental investigation of Guglielmini and Nannei (1976), CHF for copper is asymptotically unchanged for the heater thickness from 10 to 50 μm. Here, a heater thickness of 500 μm was selected to simulate the interaction between heater and liquid macrolayer without the influence of heater thickness.

Table 1 lists geometric values of the solution domain for different heat fluxes for water at atmospheric pressure.

Table 1
Geometry values of the solution domain for various heat fluxes for water at atmospheric pressure

$q \times 10^{-5}$ ($\mathrm{W\,m^{-2}}$)	3.0	4.0	5.0	6.0	7.0	8.0	9.0
δ (μm)	659.6	428.4	306.5	233.2	185.1	151.5	126.9
r_v (μm)	188.8	157.7	137.2	122.4	111.2	102.3	95.0
r_l (μm)	1566.7	1262.7	1068.1	931.6	829.9	750.8	687.3
$(r_l - r_v)/\delta$	2.1	2.6	3.0	3.5	3.9	4.3	4.7

2.4. Numerical algorithm

The SIMPLE algorithm was used to couple pressure and velocity, and the QUICK difference scheme with a second order accuracy was used for the discretization of the momentum and energy convective terms.

2.5. Grid dependence test

The grid for the solution was non-uniform, with its size decreasing geometrically toward the interfaces of stem–liquid, bubble–liquid and heater–liquid, resulting in an increasingly fine grid where large thermal and velocity gradients existed. Grid sensitivity was performed for the heat flux of 6.0×10^5 W m^{-2}. The radial versus axial grids 150×50 and 300×100 respectively yielded numerical wall superheat (the temperature difference between the heated wall and the saturation water) errors of 4.21% and 0.08% as compared to the finest radial versus axial grid 600×200. Thus the results predicted on 300×100 grid were chosen as the solutions independent of the grid size.

3. Results and discussion

Firstly, we compared our calculated boiling curve with the published experimental data. The triple-point, mass-evaporation coefficient m_{TP} for various fluid-heater surfaces is currently unknown. As mentioned previously, m_{TP} is influenced by the contact angle. The contact angle is different for different fluid-heater surface combinations and conditions. For a certain fluid-heater surface, the contact angle is only a function of the interfacial tension (Carey, 1992). As is well known, the interfacial tension is a function of temperature. In the current study, the only data considered is for the saturated water–copper combination. So the contact angle, thus m_{TP}, at triple-point can be left as a constant. As is well known, some unknown value can be obtained by using an indirect way. Since in the model only m_{TP} is undetermined as an input data for the computation, a certain m_{TP} will result in a certain computational result. We determined this coefficient in an indirect fashion by tuning one arbitrary calculated point ($q = 3.0 \times 10^5$ W m^{-2} and $T_w = 115.5$ °C in the present study) on the boiling curve to match the experimental data. This tuning yielded $m_{TP} = 4.0 \times 10^{-5}$ kg m^{-1} s^{-1} K^{-1}. The difference of the values of m_{TP} determined by the minimum heat flux of 3×10^5 W m^{-2} and the maximum heat flux 9×10^5 W m^{-2} is 3.2%. Therefore, the constant m_{TP} of 4.0×10^{-5} kg m^{-1} s^{-1} K^{-1} was used for all the heat fluxes investigated here on the boiling curve. The constant m_{TP} assumption and the same determination method of m_{TP} at triple-point was also used by Pasamehmetoglu et al. (1993). Dhir and Liaw (1989) also used this kind of indirect method to determine the value of a constant in their model.

The physical properties such as heat capacity c_p, fluid density ρ_l, dynamic viscosity μ_l, thermal conductivity k_l and thermal expansion coefficient β, which appeared in the control equations (1)–(4) are functions of temperature. Since the difference between the wall temperature and fluid temperature is not so large (about 20 K), the effect of these properties change as a function of temperature was neglected and the properties were used as constants for simplification. To investigate the effect of this simplification on the numerical results, we computed the case for the heat flux of 6×10^5 W m^{-2} with variable properties changing with temperature. Fig. 3 shows comparison of the distribution of numerical velocity along the stem–liquid interface for the constant

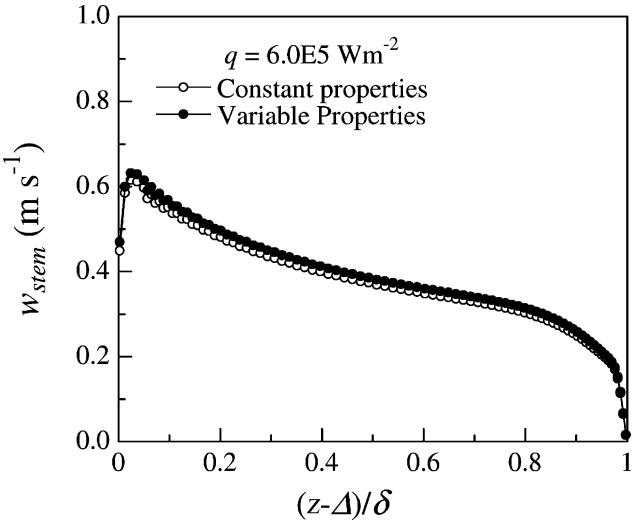

Fig. 3. Comparison of the distribution of numerical velocity along the stem–liquid interface for the constant and variable properties cases.

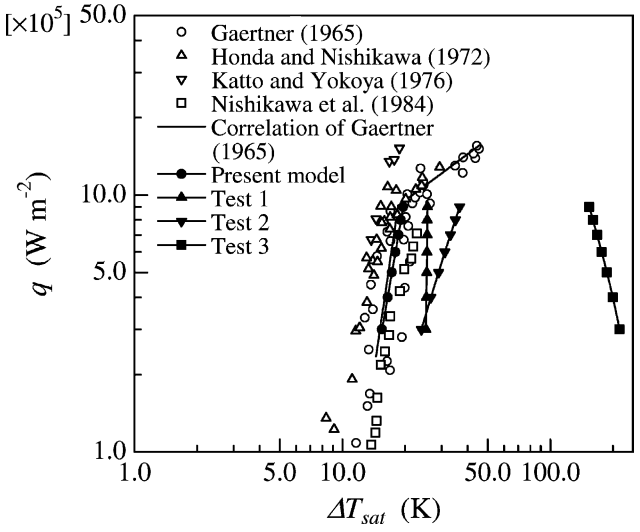

Fig. 4. Comparison of the model prediction of boiling curve with the experiments.

properties and variable properties cases. It can be seen that the maximum velocity difference between the two cases is within 3.0%. Thus the effect of property change as a function of temperature on the Marangoni+buoyancy convective flows is not great in the present study. Comparison of the numerical wall temperature shows that the constant properties assumption results in a wall temperature ($T_w = 118.007$ °C) higher by 0.2% than that for the variable properties case ($T_w = 117.817$ °C). This deviation is allowable by considering the experimental uncertainties for the wall superheat measurement. Therefore, we used constant properties in the present study for simplicity.

Fig. 4 shows the comparison of the calculated boiling curve indicated by black circles with the experimental data of Gaertner (1965), Honda and Nishikawa (1972), Katto and Yokoya (1976) and Nishikawa et al. (1984). Here, ΔT_{sat} is the wall superheat defined as the temperature difference between the heated wall and the saturation water. It can be seen from Fig. 4 that the prediction

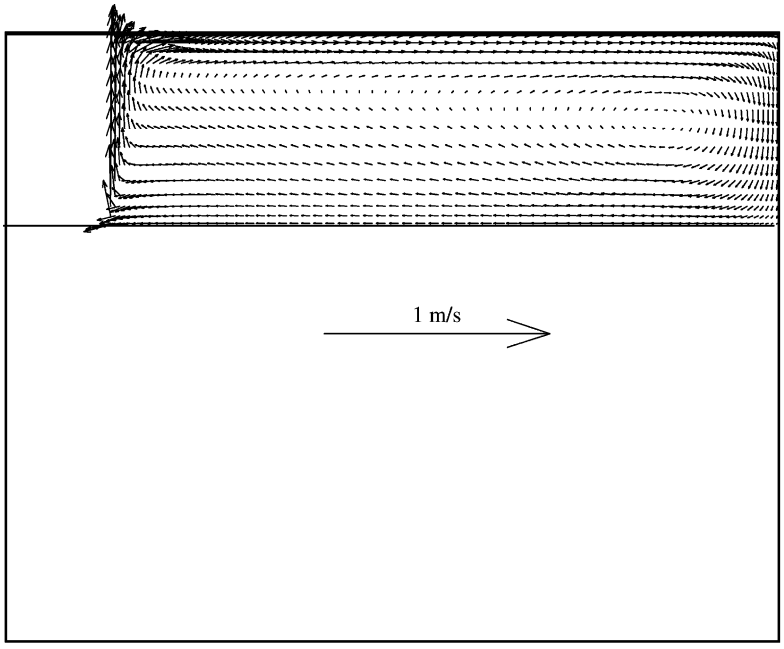

(a)

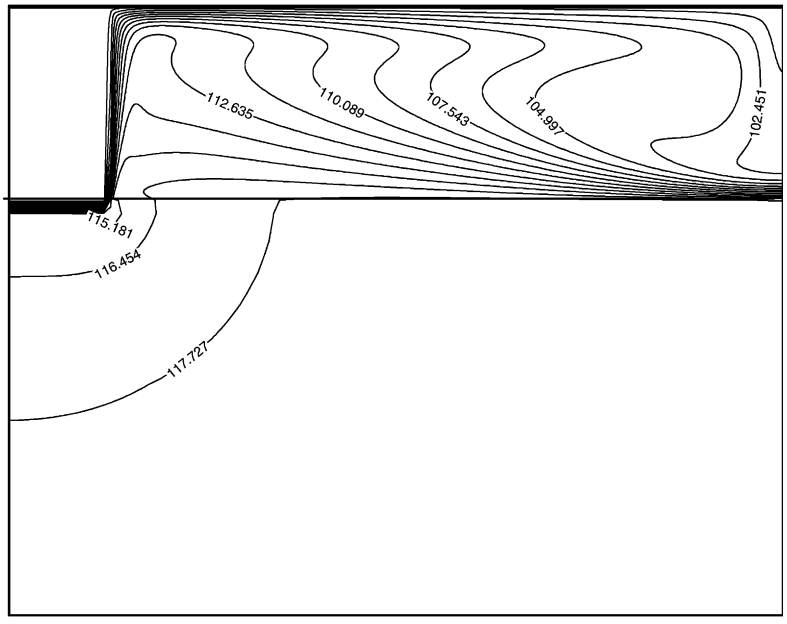

(b)

Fig. 5. Vector patterns and isotherms at the heat flux of 6.0×10^5 W m^{-2}: (a) vector patterns, (b) isotherms.

agrees very well with the correlation of Gaertner (1965) in the mushroom region. The small diameter, water-on-copper boiling data of Honda and Nishikawa (1972) and Katto and Yokoya (1976) exhibit smaller wall superheat, which is probably due to the edge effects.

Fig. 5(a) and (b) shows the vector pattern and isotherms at the heat flux of 6.0×10^5 W m^{-2} respectively. The liquid near the stem–liquid interface flows upward as expectation since the surface tension decreases with increasing temperature. The liquid near the wall is heated and is getting warmer as it flows toward the stem–liquid interface. Subsequently, as the liquid flows upward along the stem–liquid interface and then along the bubble–liquid interface, the energy is taken away by the evaporation there and the liquid is getting cooler. Then due to the fluid continuity the cooled liquid flows toward the heated wall again to extract heat from the wall. Thus this flow pattern provides an efficient heat transfer than the pure conduction. The velocity patterns and isotherms for the other studied heat fluxes are similar to those at the heat flux of 6.0×10^5 W m^{-2}.

The heat flux is transferred into the macrolayer from the heater and is taken away at the triple-point, stem–liquid and the bubble–liquid interface. Thus we have

$$Q = Q_{\mathrm{TP}} + Q_{\mathrm{stem}} + Q_{\mathrm{bubble}} \tag{19}$$

where Q is the input heat transfer rate, Q_{stem} and Q_{bubble} represent the evaporation along the stem–liquid interface and bubble–liquid interface respectively. They can be expressed as

$$\begin{aligned} Q &= 2\pi \int_0^{r_1} qr\,\mathrm{d}r = q\pi r_1^2 \\ Q_{\mathrm{stem}} &= -2\pi r_{\mathrm{v}} k_{\mathrm{l}} \int_{\Delta}^{\Delta+\delta} \left(\frac{\partial T}{\partial r}\right)_{r=r_{\mathrm{v}}} \mathrm{d}z \\ Q_{\mathrm{bubble}} &= 2\pi k_{\mathrm{l}} \int_{r_{\mathrm{v}}}^{r_1} \left(\frac{\partial T}{\partial z}\right)_{z=\Delta+\delta} r\,\mathrm{d}r \end{aligned} \tag{20}$$

In the following, we will analyze the heat transfer at the liquid–heater, stem–liquid and bubble–liquid interface.

Fig. 6(a) and (b) respectively shows the temperature and heat flux distributions along the heater upper surface for the input heat fluxes of 3.0×10^5, 6.0×10^5 and 9.0×10^5 W m^{-2}. In Fig. 6(a), the temperature firstly decreases from the axis position to the triple-point and then increases up to a given value for a specific heat flux. The temperature increases with increasing input heat flux. It can be seen in Fig. 6(b) that the largest heat flux is taken away at the triple-point, which results in the lowest temperature nearby. Since the conductivity of copper is much larger than that of the water, the area affected by the trip-point evaporation is larger for the heater than that for the macrolayer, and in a small region immediately adjacent to the right of the triple-point the heat fluxes are transferred from the liquid macrolayer to the heater.

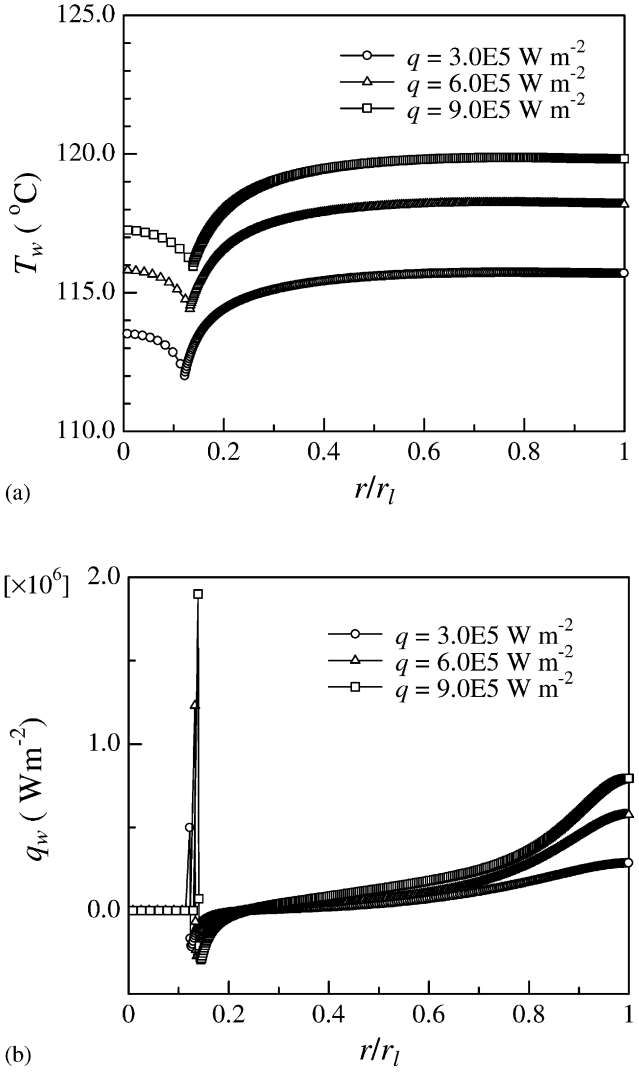

Fig. 6. Temperature and heat flux distributions along the heat upper surface: (a) temperature distribution, (b) heat flux distribution.

Fig. 7(a) and (b) respectively shows the temperature and heat flux distributions at the stem–liquid interface for the input heat fluxes of 3.0×10^5, 6.0×10^5 and 9.0×10^5 W m^{-2}. Hereinafter, we define that the sign of the heat flux added into the liquid macrolayer is positive while the sign of the heat flux taken away from the liquid macrolayer is negative. In Fig. 7(a), the temperature decreases from the heater upper surface to the bubble–liquid interface at a given heat flux. The temperature increases with increasing input heat flux. The heat flux profiles in Fig. 7(b) are in accordance with the temperature profiles shown in Fig. 7(a).

Fig. 8(a) and (b) respectively shows the temperature and heat flux distributions at the bubble–liquid interface for the input heat fluxes of 3×10^5, 6×10^5 and 9×10^5 W m^{-2}. In Fig. 8(a), the temperature firstly increases to the maximum value and then decreases at a given heat flux. The temperature increases with increasing input

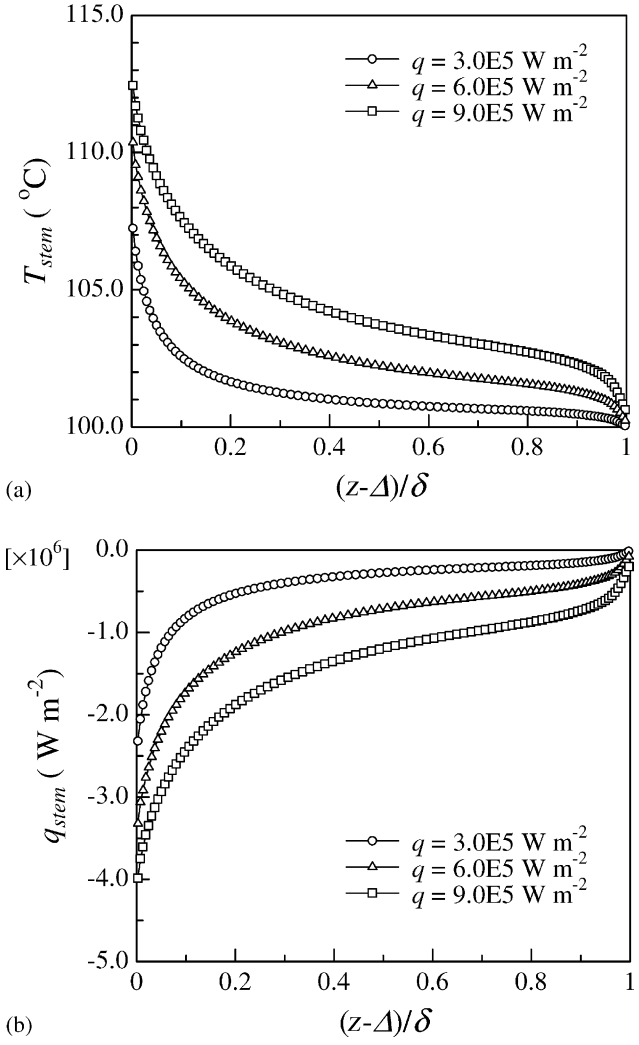

Fig. 7. Temperature and heat flux distributions at the stem–liquid interface: (a) temperature distribution, (b) heat flux distribution.

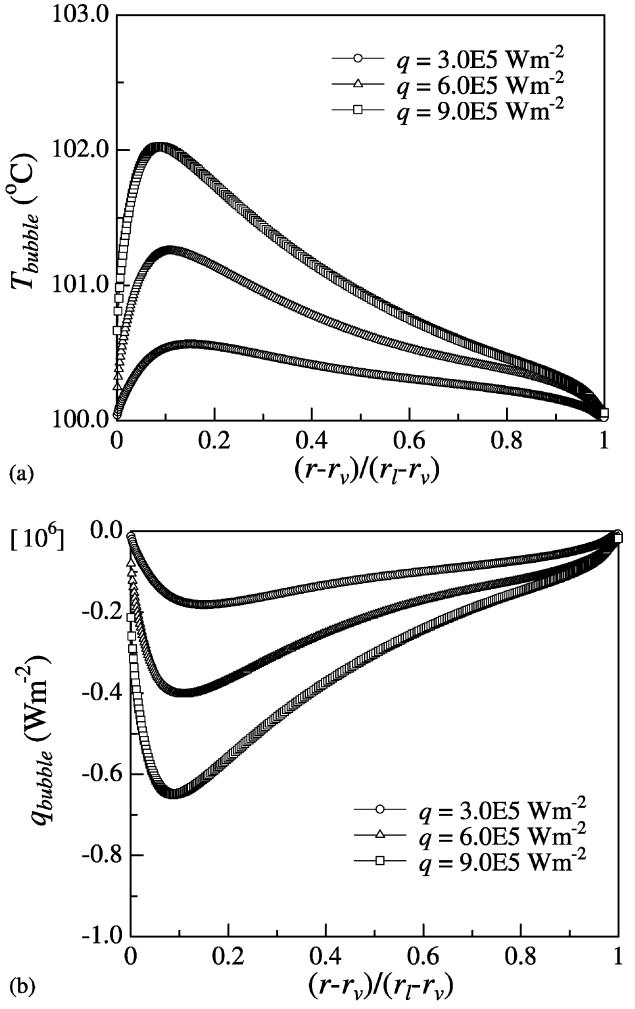

Fig. 8. Temperature and heat flux distributions at the bubble–liquid interface: (a) temperature distribution, (b) heat flux distribution.

heat flux. The heat flux profiles in Fig. 8(b) are in accordance with the temperature profiles shown in Fig. 8(a).

Table 2 lists the numerical results for the Marangoni number, the wall temperature and the evaporation fraction of the triple-point, stem–liquid interface and bubble–liquid interface for various heat fluxes. Here, Marangoni number is defined as

$$Ma = \frac{-\partial\sigma/\partial T\,\delta\Delta T_{\mathrm{sat}}}{\mu\alpha} \tag{21}$$

From the table, we can see that Marangoni number is very large for the generation of Marangoni convection, suggesting that neglecting Marangoni convection be not suitable in the analysis. For evaluating the individual evaporation contribution of the triple-point, stem–liquid interface and bubble–liquid interface, we define

$$f_{\mathrm{TP}} = Q_{\mathrm{TP}}/Q, \quad f_{\mathrm{stem}} = Q_{\mathrm{stem}}/Q, \quad f_{\mathrm{bubble}} = Q_{\mathrm{bubble}}/Q \tag{22}$$

The evaporation at the triple-point plays a very important role in the heat transfer with a weighting fraction

Table 2
Numerical results for various heat fluxes for water at atmospheric pressure

$q \times 10^{-5}$ (W m^{-2})	3.0	4.0	5.0	6.0	7.0	8.0	9.0
$Ma \times 10^{-4}$	4.4	3.0	2.3	1.8	1.5	1.2	1.1
T_w (°C)	115.5	116.5	117.3	118.0	118.6	119.1	119.6
f_{TP} (%)	55.7	58.0	59.9	61.4	62.6	63.7	64.7
f_{stem} (%)	13.7	12.1	10.9	10.0	9.2	8.5	8.0
f_{bubble} (%)	30.6	29.9	29.2	28.6	28.2	27.8	27.3

ranging from 56% up to 65% over the heat flux ranges investigated. The relative evaporation at the bubble–liquid interface is about 30% and the relative evaporation at the stem–liquid interface decreases from 13.7% at the heat flux of 3.0×10^5 W m^{-2} to 8.0% at the heat flux of 9.0×10^5 W m^{-2} due to the reduction of the macrolayer thickness with the increase of the heat flux.

To further assess the relative influence of the triple-point (microlayer) evaporation and Marangoni convection on the heat transfer, we conducted the following three additional tests:

Test 1, the Marangoni convection was shut off in our model;
Test 2, the triple-point evaporation coefficient was set to zero in our model;
Test 3, the combination of Tests 1 and 2.

Fig. 9 shows the typical isotherms in the macrolayer region at the heat flux of 6.0×10^5 W m^{-2} for the three additional tests. It can be seen that the stratified temperature distribution smoothly decreases from the heated wall to the interfaces of stem–liquid and bubble–liquid

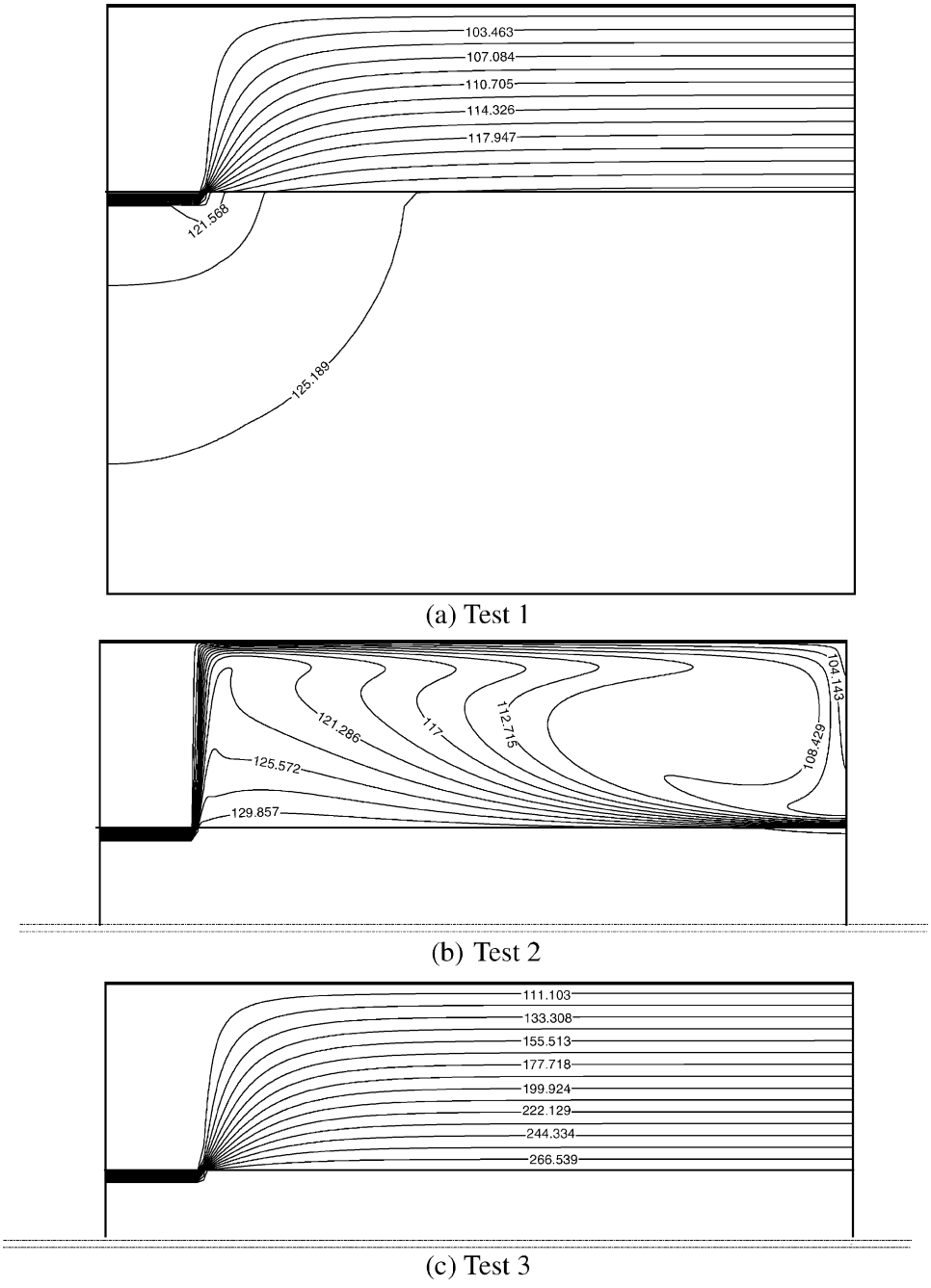

Fig. 9. Isotherms at the heat flux of 6.0×10^5 W m^{-2} for the test cases: (a) Test 1, (b) Test 2, (c) Test 3.

in Tests 1 and 3, whereas the heat transfer path is distorted in Test 2 due to the Marangoni convection.

Tables 3–5 give the numerical results for the above three additional tests for various heat fluxes. The predicted boiling curves of Tests 1, 2 and 3 are also shown in Fig. 4 for comparison. It can be clearly seen in Tables 3–5 and Fig. 4 that the calculated wall temperatures in the three additional tests increase in the order of Tests 1, 2 and 3, which indicates the decreasing relative contributions in the order of the microlayer evaporation, Marangoni covection and pure conduction and evaporation of the macrolayer. The highest wall temperature (250–315 °C) obtained in Test 3 indicates that the pure conduction has not the capability to extract the heat flux efficiently from the heater surface to the vapor–liquid interface for evaporation. The wall temperature decreases with increasing heat flux due to the reduction of the macrolayer thickness, showing an unreasonable strongly backward boiling curve in Fig. 4. In Test 2, the wall temperature decreases greatly by introducing Marangoni convection in the macrolayer region as compared to Test 3, indicating that Marangoni-induced thermo-capillary driven flow constitutes a highly efficient heat removal mechanism. The overprediction of the wall temperature in Test 2 suggests Marangoni convection in the macrolayer region not be solely responsible for the heat transfer rates observed in nucleate boiling. Both Tests 2 and 3 show that the major heat transfer occurs at the bubble–liquid interface (see f_{bubble} in Tables 4 and 5). Although the triple-point mass-evaporation coefficient in Test 1 can be tuned to a certain value to match the calculated boiling curve with the experimental data, this is believed to exaggerate the microlayer evaporation (see f_{TP} in Tables 2 and 3) by neglecting Marangoni convection which does exist in the macrolayer. Thus the new model developed in the present study should be more reasonable for revealing the full heat transfer mechanisms and their relative contributions in the mushroom region of saturated pool nucleate boiling.

As mentioned previously, a value of 0.04 was adopted for the evaporation coefficient E in the present study. A sensitivity study of E on the calculated results was carried out and the effect of the evaporation coefficient E on the calculated wall temperature T_{w} at the heat flux of 6.0×10^5 W m^{-2} is shown in Fig. 10. It can be seen that T_{w} increases with increasing E. Fig. 11 shows the vector pattern in the macrolayer region at the heat flux of 6.0×10^5 W m^{-2} for $E = 0.5$. We can see that the intensity of Marangoni convection in the macrolayer region becomes weak as compared to the case for $E = 0.04$ shown in Fig. 5(a). It is the decrease of the intensity of Marangoni convection that leads to the increase of T_{w} with increasing E. Table 6 lists the numerical results for the Marangoni number, the wall temperature and the evaporation fraction of the triple-point, stem–liquid interface and bubble–liquid interface at $E = 1.0$ and $q = 6.0 \times 10^5$ W m^{-2}. It can be seen in Table 6 that the evaporation fraction of stem–liquid interface and bubble–liquid interface decreases as compared to the case of $E = 0.04$ and $q = 6.0 \times 10^5$ W m^{-2} (see Table 2) due to the decrease of the intensity of Marangoni convection.

Table 3
Numerical results for various heat fluxes for water at atmospheric pressure (Test 1)

$q \times 10^{-5}$ (W m^{-2})	3.0	4.0	5.0	6.0	7.0	8.0	9.0
$Ma \times 10^{-4}$	7.1	4.7	3.3	2.6	2.0	1.7	1.4
T_{w} (°C)	125.21	125.35	125.44	125.52	125.56	125.59	125.62
f_{TP} (%)	88.8	87.7	86.8	85.9	85.1	84.3	83.6
f_{stem} (%)	3.2	2.9	2.6	2.4	2.2	2.1	2.0
f_{bubble} (%)	8.0	9.4	10.6	11.7	12.7	13.6	14.4

Table 4
Numerical results for various heat fluxes for water at atmospheric pressure (Test 2)

$q \times 10^{-5}$ (W m^{-2})	3.0	4.0	5.0	6.0	7.0	8.0	9.0
$Ma \times 10^{-4}$	6.8	4.9	3.8	3.1	2.6	2.3	2.0
T_{w} (°C)	124.0	126.6	129.0	131.1	133.1	134.9	136.6
f_{stem} (%)	29.3	27.1	25.4	23.9	22.6	21.5	20.4
f_{bubble} (%)	70.7	72.9	74.6	76.1	77.4	78.5	79.6

Table 5
Numerical results for various heat fluxes for water at atmospheric pressure (Test 3)

$q \times 10^{-5}$ (W m^{-2})	3.0	4.0	5.0	6.0	7.0	8.0	9.0
$Ma \times 10^{-4}$	61.0	36.8	24.6	17.7	13.3	10.4	8.4
T_{w} (°C)	315.3	300.2	287.2	276.8	268.0	260.4	253.9
f_{stem} (%)	32.1	26.2	22.2	19.2	16.9	15.1	13.6
f_{bubble} (%)	67.9	73.8	77.8	80.8	83.1	84.9	86.4

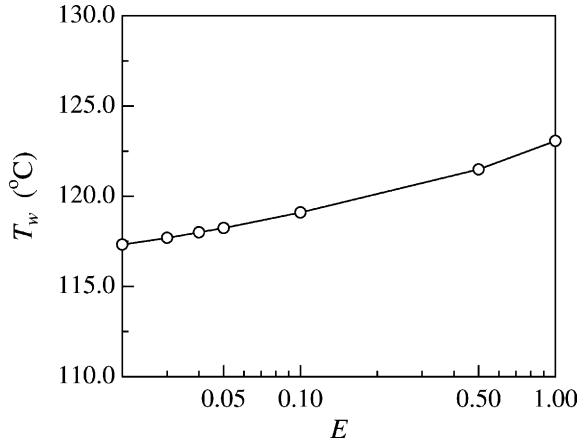

Fig. 10. Effect of the value of E on the calculated wall temperature T_w.

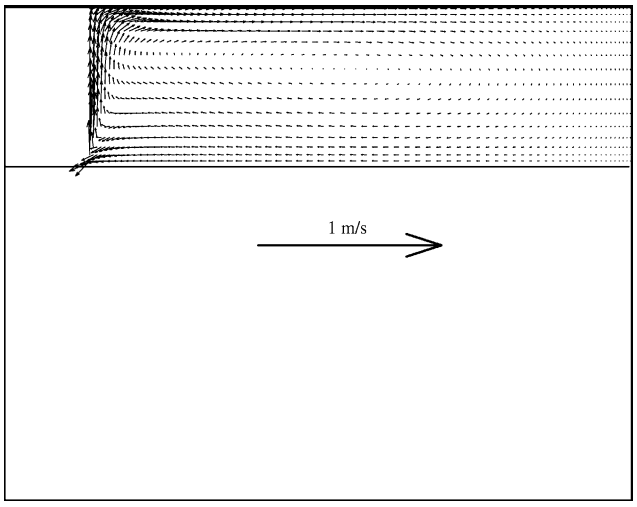

Fig. 11. Vector pattern at the heat flux of 6.0×10^5 W m^{-2} for $E = 0.5$.

Table 6
Numerical results for water at atmospheric pressure with $E = 1.0$ at the heat flux of 6.0×10^5 (W m^{-2})

$Ma \times 10^{-4}$	T_w (°C)	f_{TP} (%)	f_{stem} (%)	f_{bubble} (%)
1.3	123.3	79.4	7.6	13.0

From Table 6, we can also see that the calculated T_w ($= 123.06$ °C) at $E = 1.0$ is about 2.2 K lower than that in Test 1, in which the Marangoni convection was not considered (see Table 3, $T_w = 125.52$ °C), indicating that the Marangoni convection still plays an important role even if the value of E reaches its maximum value of unity. Therefore, the Marangoni convection should be considered in revealing the highly efficient heat transfer mechanisms in the vapor mushroom region of saturated nucleate pool boiling irrespective of the value of E. Considering the actual conditions in most engineering systems as mentioned previously, a value of 0.04 for E, as recommended by Ma and Pan (1999a), is reasonable for the present model computation.

4. Conclusions

A new model was developed for the heat transfer and fluid flow in the vapor mushroom region of saturated nucleate pool boiling in which three heat transfer mechanisms were incorporated, the conduction and evaporation in the microlayer region, the conduction and evaporation in the macrolayer region and Marangoni convection in the macrolayer region. The main conclusions can be itemized as follows:

(1) The heat flux can be efficiently transferred to the vapor–liquid interface by the Marangoni convection.
(2) From the new proposed model predictions, the evaporation at the triple-point plays a very important role in the heat transfer with a weighting fraction of about 60% over the heat flux ranges investigated, and the relative evaporations at the bubble–liquid interface and the stem–liquid interface are about 30% and 10% respectively.
(3) Overprediction of the wall superheat in the additional tests in which Marangoni convection or/and microlayer evaporation were not considered further indicates that both the Marangoni convection and microlayer evaporation play important roles in the mushroom region of saturated pool nucleate boiling heat transfer.

Acknowledgement

We appreciate helpful discussions with Dr. Y. Kawaguchi at National Institute of Advanced Industrial Science and Technology.

References

Bhat, A.M., Prakash, R., Saini, J.S., 1983a. On the mechanism of macrolayer formation in nucleate pool boiling at high heat fluxes. Int. J. Heat Mass Transfer 26, 735–740.
Bhat, A.M., Prakash, R., Saini, J.S., 1983b. Heat transfer in nucleate pool boiling at high heat fluxes. Int. J. Heat Mass Transfer 26, 833–840.
Bhat, A.M., Saini, J.S., Prakash, R., 1986. Role of macrolayer evaporation in pool boiling at high heat flux. Int. J. Heat Mass Transfer 29, 1953–1961.
Carey, V.P., 1992. Liquid–Vapor Phase-Change Phenomena. Hemisphere Publishing Corporation.
Chyu, M.-C., 1989. Evaporation of macrolayer in nucleate boiling near burnout. Int. J. Heat Mass Transfer 30, 1531–1538.
Collier, J.G., 1972. Convective Boiling and Condensation. McGraw-Hill, New York, NY, vol. 322.
Dhir, V.K., Liaw, S.P., 1989. Frame work for a unified model for nucleate and transition pool boiling. Trans. ASME J. Heat Transfer 111, 739–746.
Gaertner, R.F., 1965. Photographic study of nucleate pool boiling on a horizontal surface. Trans. ASME J. Heat Transfer 87, 17–29.
Guglielmini, G., Nannei, E., 1976. On the effect of heating wall thickness on pool boiling burnout. Int. J. Heat Mass Transfer 19, 1073–1075.

Haramura, Y., Katto, Y., 1983. A new hydraulic model for critical heat flux, applicable widely to both pool and forced convection boiling on submerged bodies in saturated liquids. Int. J. Heat Mass Transfer 26, 389–399.

Honda, H., Nishikawa, K., 1972. Experimental study of transition boiling heat transfer mechanism (2nd Report, Vapor mass behavior and heat transfer). Trans. JSME 38, 177–187.

Hsu, Y.Y., Graham, R.W., 1986. Transport process in boiling and two-phase systems including near-critical fluids. American Nuclear Society, La Grange Park, IL, pp. 55–58.

Iida, Y., Kobayasi, K., 1969. Distribution of void fraction above a horizontal heating surface in pool boiling. Bull. JSME 12, 283–290.

Jairajpuri, A.M., Saini, J.S., 1991. A new model for heat flow through macrolayer in pool boiling at high heat fluxes. Int. J. Heat Mass Transfer 34, 1579–1591.

Kao, Y.S., Kenning, D.B.R., 1972. Thermocapillary flow near a hemispherical bubble on a heated wall. J. Fluid Mech. 53, 715–735.

Katto, Y., Yokoya, S., 1976. Behavior of vapor mass in saturated nucleate and transition boiling. Heat Transfer, Jap. Res. 5, 45–65.

Lay, J.H., Dhir, V.K., 1995. Shape of a vapor stem during nucleate boiling of saturated liquids. Trans. ASME J. Heat Transfer 117, 395–402.

Ma, K.T., Pan, C., 1999a. Thermo-capillary driven flow in macrolayer at high wall heat fluxes. Int. J. Numer. Methods Heat Fluid Flow 9, 788–808.

Ma, K.T., Pan, C., 1999b. The effect of heated wall thickness and materials on nucleate boiling at high heat flux. Int. Comm. Heat Mass Transfer 26, 1103–1114.

Nishikawa, K., Fujita, Y., Uchida, S., Ohta, H., 1984. Effect of surface configuration on nucleate boiling heat transfer. Int. J. Heat Mass Transfer 27, 1559–1571.

Pan, C., Hwang, J.Y., Lin, T.L., 1989. The mechanism of heat transfer in transition boiling. Int. J. Heat Mass Transfer 32, 1337–1349.

Pan, C., Lin, T.L., 1989. Marangoni flow on pool boiling near critical heat flux. Int. Comm. Heat Mass Transfer 16, 475–486.

Pasamehmetoglu, K.O., Chappidi, P.R., Unal, C., Nelson, R.A., 1993. Saturated pool nucleate boiling mechanisms at high heat fluxes. Int. J. Heat Mass Transfer 36, 3859–3868.

Pasamehmetoglu, K.O., Nelson, R.A., 1987. The effect of Helmholtz instability on the macrolayer thickness in vapor mushroom region of nucleated pool boiling. Int. Comm. Heat Mass Transfer 14, 709–720.

Paul, B., 1962. Compilation of evaporation coefficients. ARS J. 32, 1321–1328.